Disorder-induced decoupled surface transport channels in thin films of doped topological insulators

Hanbum Park, Jimin Chae, Kwangsik Jeong, Hyejin Choi, Jaehun Jeong, Dasol Kim, and Mann-Ho Cho*
Department of Physics, Yonsei University, Seoul 03722, Republic of Korea

(Received 1 February 2018; published 12 July 2018)

Nonideal topological insulator (TI) films in which the bulk states are not insulating due to unintentional doping exhibit strong surface–bulk coupling. Such surface–bulk coupling can further induce intersurface coupling that affects the electrical conductivity of the TI films through a quantum interference effect known as weak antilocalization. Increased understanding and control of intersurface coupling is therefore crucial for the use of TI-based quantum devices. In this report on the transport properties of doped Bi_2Se_3 films under perpendicular and parallel magnetic fields, we observe a crossover between coupled and decoupled surface channels that is mediated by intentional disorder controlled by a post-annealing process. The intentional disorder causes the surface state carriers to rapidly lose their quantum phase and coherence, and as a result, more disordered Bi_2Se_3 films exhibit a shorter penetration depth of the surface state into the bulk states and weaker intersurface coupling, even though stronger surface–bulk coupling is expected. In previous studies, the role of disorder has generally been considered by determining its effect on surface–bulk scattering, but our results indicate that the role of disorder must be considered as a source of decoherence.

DOI: 10.1103/PhysRevB.98.045411

I. INTRODUCTION

Dirac-like surface states within the bulk band gap of three-dimensional (3D) topological insulators (TIs) are robust against structural disorder owing to the existence of the Kramers' degeneracy at the Dirac point [1,2]. Since this topological surface state (TSS) is a spin–momentum locked helical state arising from strong spin–orbit coupling effects, backscattering is prohibited without breaking the time-reversal symmetry of the system [1–3]. This novel property of TSSs suggests that TI-based quantum devices have great potential in the fields of spintronics [4–6] and quantum computation [1,7]. However, utilizing the surface transport channel is usually hindered by topologically trivial bulk channels arising from unintentional doping during the synthesis of TI materials [8], such as Bi_2Se_3, Bi_2Te_3, and Sb_2Te_3. Furthermore, the bulk states mediate between the top and bottom TSSs of the doped TI film, causing them to be indirectly coupled even for film thicknesses greater than 6 quintuple layers (QL, where 1 QL $\sim$ 9.54 Å), which is the critical thickness for direct coupling reported in electronic structure calculations [9,10], angle-resolved photoemission spectroscopy (ARPES) [11,12], and transport measurement [13]. This indirect intersurface coupling affects the quantum correction to the electrical conductivity through a mechanism known as the weak antilocalization (WAL) effect [14].

In a disordered 3D TI film, since scattering at any angle except backscattering is allowed, the trajectories of a transported carrier can form a closed loop after a series of scatterings. The surface carriers of a TI have a π Berry phase accumulated along the closed loop, which gives rise to a positive correction to the conductivity owing to the destructive quantum interference between time-reversed trajectories [2,15]. Thus, WAL effects from both the top and bottom TSSs in insulating TI films—whose Fermi level is located in the bulk band gap—contribute independently to the conductivity. However, in doped TI films, the surface carriers are scattered into the bulk states by phonons and disorders, and this scattering is called surface–bulk coupling [16,17]. Furthermore, this surface–bulk coupling can also connect the top and bottom topological surfaces without decoherence when the thickness of TI film is sufficiently thin, which is called intersurface coupling [14]. In this case, the WAL effects of the TSSs are no longer independent and the two coherent surface channels form an effectively single coherent channel. In addition, while the TSS wavefunction of the insulating TI film is highly localized at the surface of the film, the wavefunction of the doped TI film is distributed along the c axis [18]. In other words, the TSS wavefunction of a doped TI film has a longer decay length. Moreover, Tkachov and Hankiewicz have reported that the TSS wavefunction decay length in TI films is equivalent to the penetration depth of the TSS into the bulk states and significantly affects the strength of the WAL effect [19].

The improved interpretation and control of intersurface coupling is thus crucial to the successful use of TI-based quantum devices. For this reason, a great deal of intensive research on surface–bulk and intersurface coupling has been performed [16,17]; the crossover between coupled and decoupled TSSs has been observed through control of the gate voltage [20–22], the modulation of the film thickness [23,24], and Cu doping [14]. In this report we introduce a new mechanism to induce decoupled surface channels in doped Bi_2Se_3 films, namely, by intentional disorder controlled by a post-annealing process. From the results of transport studies under perpendicular and parallel magnetic fields, we investigate the relationship between the penetration depth and the extent of disorder present in the film. Since the disorder acts as a cause of surface–bulk coupling, more disordered

*mh.cho@yonsei.ac.kr

films are expected to exhibit stronger surface–bulk coupling, which can lead to stronger intersurface coupling. However, disorder also causes the electrons of the TSSs to rapidly lose their quantum phase and coherence as they tunnel to the opposite TSS. Consequently, we observe that more disordered Bi_2Se_3 films exhibit shorter penetration depths and weaker intersurface coupling, resulting in the emergence of decoupled surface transport channels.

II. EXPERIMENTAL

To acquire various extents of structural disorder in our Bi_2Se_3 thin films, we controlled the temperature in the post-annealing crystallization process of $[Bi\,(4.8\,Å)/Se\,(18.4\,Å)]_n$ multilayers initially grown by thermal evaporation on a-SiO_2/p-doped Si substrates in an ultra-high vacuum (UHV) chamber [25]. The annealing temperature was raised by ∼5 °C/min and maintained at the target temperature for 20 min, which was a sufficient period for the annealing time not to affect the extent of disorder. After that, the heating was immediately stopped for the cooling process which was maintained for 2 h, ultimately reaching room temperature. Further details regarding our growth method are provided in our previous work [26], and the films obtained after the annealing process were confirmed to be of high quality. The extent of disorder was investigated by cross-sectional STEM imaging using a JEOL ARM200F field emission gun transmission electron microscope (FEG-TEM/STEM) with a hexapole corrector (CEOS GmbH), HR-XRD patterns obtained with the 5A beam line of the Pohang Accelerator Laboratory (PAL, Pohang, Korea), and micro-Raman spectroscopy using a Horiba Lab Ram ARAMIS with a 532-nm-wavelength Nd:YAG laser. A c-axis-oriented crystalline structure could be grown on the substrate for annealing temperatures larger than 175 °C. The most disordered crystalline TI film was thus acquired by post-annealing at 175 °C, and the films gradually became more ordered as the annealing temperature was increased up to 275 °C. To inhibit surface oxidation, which can induce surface band-bending and significantly affects the properties of surface states [16,27,28], the Bi_2Se_3 films were capped with a Se layer with a thickness of ∼20 nm. We assumed that the transport properties and surface–bulk coupling of the top and bottom surfaces were virtually equivalent for studying the WAL effect, which was therefore analyzed based on the assumption that the phase coherence length and the surface penetration depth are the same between the surfaces [29]. The transport properties of the TI films were measured with a four-point probe using standard Hall bar configurations and fabricated with physical masks 100 μm in size. To study and clarify the quantum corrections to the electrical conductivity, our magnetoresistance measurements were performed using magnetic fields with magnitudes of up to 9 T applied perpendicularly and parallel to the films over a temperature range of 2–300 K using a physical property measurement system (PPMS).

III. RESULTS AND DISCUSSION

A. Modulation of disorder

The post-annealing process in the growth of the TI film is a key factor for the fabrication of highly crystalline Bi_2Se_3 thin films and the formation of TSSs [25]. Although TSSs are robust against disorder, a TSS cannot emerge when the extent of disorder is extremely high. The amount of structural disorder following the post-annealing process and its relationship with the topological transport properties of the TSS (which depend on the disorder) were thus investigated. Scanning transmission electron microscopy (STEM) cross-sectional images of Bi_2Se_3 thin films annealed at 175 °C and 275 °C are presented in Figs. 1(a) and 1(b), respectively. Both films are seen to comprise a layered crystalline structure along the c-axis direction (which is the typical structure of a 3D TI film), but the extent of disorder is clearly different. The film annealed at 175 °C is tilted with respect to the surface of substrate and indicates relatively more grain boundaries. In contrast, the film annealed at 275 °C is highly oriented along the c axis and indicates large grains approximately 100 nm in size (see Fig. S1 in the Supplemental Material [30]).

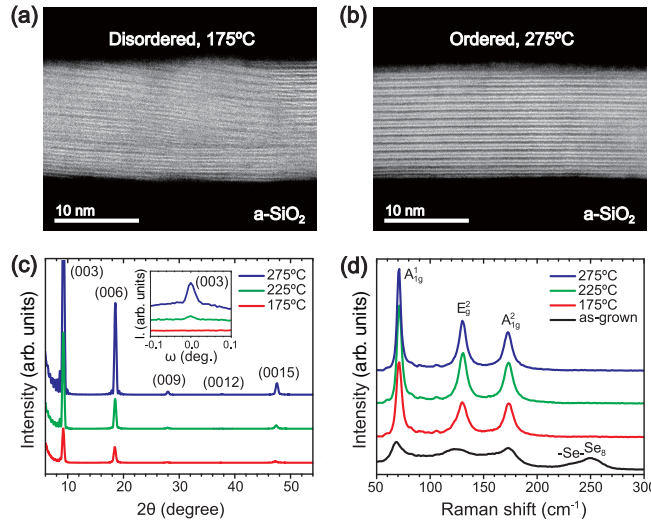

FIG. 1. Structural analyses of the Bi_2Se_3 thin films for different annealing temperatures. Cross-sectional STEM images of the films annealed at (a) 175 °C and (b) 275 °C, respectively. The layered structure of the Bi_2Se_3 films are clearly evident and the film thickness is 14 QL. (c) HR-XRD patterns (θ–2θ scans) of the films. Only the (003) peak families corresponding to the single phase Bi_2Se_3 are shown. The inset shows the rocking curve scan (ω scan) of the (003) peak. (d) Raman spectra of the films. After post-annealing, only the vibrational modes of the single phase Bi_2Se_3 are evident. The results of these structural analyses indicate that the extent of disorder decreases as the annealing temperature increases.

The long-range order of the Bi_2Se_3 thin films was evaluated by high-resolution x-ray diffraction (HR-XRD) measurements. After annealing the films at temperatures above 175 °C, the films formed a single Bi_2Se_3 rhombohedral crystal phase structure and exhibited Laue oscillations that were sensitive to crystalline disorder [31], as shown in Fig. 1(c) (also see Fig. S2 in the Supplemental Material [30]). As the annealing temperature increases, we see that the XRD intensities clearly increase and the oscillations become more distinct, which indicates that the structural order of the crystal is improved. In addition, a rocking curve scan (ω scan) was performed to evaluate the c-axis orientation in closer detail, as shown in the inset of Fig. 1(c). The sharp rocking curve peak corresponding

to the (003) diffraction peak appears in films annealed at 225 °C and 275 °C with full width at half maximum (FWHM) values of $\Delta\omega = 0.0264$ and $\Delta\omega = 0.0207$, respectively (determined using the Voigt equation), while the peak does not appear in the film annealed at 175 °C. Thus, although the film annealed at 175 °C is composed of a single Bi_2Se_3 phase, the crystalline grains are slightly tilted and twisted with respect to the surface, which leads to the films having short-range order. As the annealing temperature is increased, the films become highly ordered and comprise larger crystalline grains, which is consistent with the STEM images presented in Figs. 1(a) and 1(b).

Figure 1(d) shows the Raman spectra of the Bi_2Se_3 films for different annealing temperatures. The broad band of the amorphous phase in the 100–200 cm^{-1} region and the peaks of –Se–Se– chains (~230 cm^{-1}) and Se_8 rings (~250 cm^{-1}) are evident in the as-grown film. After the post-annealing process, the broad band transforms into a narrow band corresponding to the vibrational modes of the single Bi_2Se_3 phase and the excess Se peaks disappear. In addition, the intensity ratio of the in-plane vibrational mode to the out-of-plane mode, $I_{E_g^2}/I_{A_{1g}}$, gradually increases, which indicates that the crystallinity difference in directions is also changed during the annealing process. Overall, the results of our structural analyses indicate that the extent of disorder decreases as the annealing temperature is increased.

The phase transition from an amorphous to crystalline Bi_2Se_3 thin film structure begins at the post-annealing temperature of 125 °C, and that the structural transition dramatically affects the transport properties of the films. Indeed, the resistance of highly insulating as-grown film decreases during the phase transition by five orders of magnitude (see Fig. S4 in the Supplemental Material [30]). In addition, the change in film resistance with different annealing temperatures are presented as a function of the measurement temperature in Fig. 2(a). The resistance of the crystalline films decreases with decreasing temperature owing to the reduction of phonon scattering, which is the typical metallic behavior of a doped TI [32]. In contrast, the amorphous film annealed at 150 °C that shows a highly disordered structure exhibits insulating behavior. This tendency of the resistance as a function of temperature is reversed at about 20 K, which is correlated with the WAL effect and electron–electron interactions (EEIs) [33]. In the low temperature regime, the phase coherence length (l_ϕ) becomes larger than the mean free path of electrons (l_e)—which is called the quantum diffusive regime [15]—and the WAL effect can emerge. Moreover, the EEI becomes a dominant factor in breaking the coherence of two-dimensional (2D) systems [34,35].

Hall measurements of 20-QL-thick Bi_2Se_3 films and their fitted results are presented in Figs. 2(b) and 2(c), respectively. The almost linear behavior of the Hall resistance with respect to the magnetic field indicates that the transport is dominated by a single type of carrier [13]. In this case, we obtained the sheet carrier densities (n_s) and mobility (μ_H) using only a single carrier model of the low field strength data because of the low reliability of the two-carrier fitting including surface and bulk carriers [36]. It is reasonable to assume from previous work [37] that the 2D electron gas induced by downward band-bending due to the difference in work function

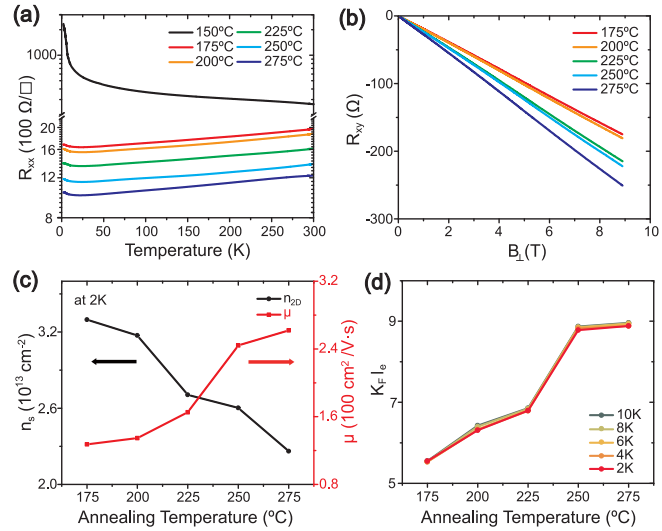

FIG. 2. Transport properties of the Bi_2Se_3 thin films for different annealing temperatures. (a) Temperature dependence of the sheet resistance in the 2–300 K range. The crystalline films exhibit the typical metallic behavior of doped TI films, while the amorphous film annealed at 150 °C exhibits insulating behavior. (b) Hall measurements at 2 K and (c) fitted results for the sheet carrier densities and mobilities. On account of the almost linear behavior of the Hall resistance with respect to the magnetic field, the results are fitted with a single carrier model of the low field data. (d) Ioffe–Regel criterions for different annealing temperatures. These results indicate that the extent of disorder decreases as the annealing temperature is increased.

is not present at the interface between the Bi_2Se_3 film and SiO_2/p-doped Si substrate in our sample. The highly doped Bi_2Se_3 film on the p-doped Si substrate is believed instead to exhibit upward band-bending. The sheet carrier densities of all films reported here are within the range of typical bulk carrier densities ($>10^{13}$ cm^{-2}) in doped Bi_2Se_3 thin films [32,38].

Since the more ordered film has a smaller number of defects and larger grains, the mobility increases as the annealing temperature is increased, while the carrier density decreases. Moreover, we can obtain the mean free paths in the films with the relations, $l_e = (\hbar\mu_H/e)k_F$ and $k_F \sim (3\pi^2 n_{3D})^{1/3}$, where k_F is the Fermi momentum. Because the transport is dominated by bulk carriers, here we use the 3D model. Using these relations, we find that the more ordered film has a longer mean free path. The longest mean free path we observed, $l_e =$ 12.4 nm for the most ordered film, is obtained at 2 K (see Fig. S5 in the Supplemental Material [30]). In addition, the Ioffe–Regel criterions with the film's transport properties are presented in Fig. 2(d) and were used to evaluate the extent of the disorder. According to the Ioffe–Regel criterion [39], $k_F l_e \ll 1$ indicates a strongly disordered system while $k_F l_e \gg 1$ indicates a weakly disordered system. The obtained $k_F l_e$ of all the crystalline films correspond to the weakly disordered regime that is required to use typical quantum interference theory [40], and $k_F l_e$ increases as the annealing temperature is increased. Thus, the changes in n_s and μ_H also indicate that the extent of disorder decreases as the annealing temperature is increased.

However, the obtained mean free path is valid only in a direction parallel to the film plane owing to the anisotropic Fermi surface [41]. To thoroughly investigate the perpendicular motion of carriers that can induce intersurface coupling, this anisotropic behavior of carriers should be considered [42]. We therefore estimated the mean free path in the perpendicular direction ($l_{e,\perp}$) by comparing the carrier mobility in the perpendicular and parallel directions with the results of optical and electrical investigations of n-type Bi_2Se_3 single crystals [41], and determined that on average, $l_{e,\perp} \approx l_e/3$. In addition, we also note that the diffusion constant and phase coherence length also exhibit anisotropic behavior. The diffusion constant in a 3D system is defined as $D = (\hbar k_F/3m_e)l_e$, and the phase coherence length as $l_\phi = \sqrt{\tau_\phi D}$, where m_e is the electron mass and τ_ϕ is the phase coherence time [43]. As we shall discuss in the following, these anisotropic properties are important for our analysis of the magneto-conductivity (MC) under a parallel magnetic field [42].

B. Crossover from coupled to decoupled surface channels

To investigate how the WAL effect depends on the disorder, we performed magnetoresistance measurements in the low temperature regime. When the magnetic field is applied perpendicularly to the closed loop, the time reversal symmetry is broken and the carriers acquire an additional phase on account of the Aharonov–Bohm effect. These changes then break the coherence and suppress the quantum interference effects [39,44,45]. Thus, the WAL effect of the TSS is sensitive to the perpendicular magnetic field and gives rise to a sharp cusp in the resistance at low magnetic fields. The normalized change in the resistance of 20-QL-thick Bi_2Se_3 films for various annealing temperatures under a perpendicular magnetic field is presented in Fig. 3(a). All crystalline films exhibit a sharp WAL cusp, while the amorphous film exhibits a weak localization (WL) cusp in a narrow magnetic field region in addition to the WAL cusp, as shown in the inset of Fig. 3(a). The film annealed at 275 °C shows unusual negative magnetoresistance at high field strength, which seems that the film exhibits the WL effect. At low field strength, longitudinal MC can be expressed approximately as $\sigma_{xx} \approx 1/R_{xx}$. However, due to the contribution from the Hall effect, MC should be expressed at high field strength as $\sigma_{xx} = R_{xx}/(R_{xx}^2 + R_{xy}^2)$. As such, positive MC is not observed as shown in Fig. 3(b), which was obtained with the latter equation. Thus, while the film does not exhibit the WL effect it may just show negative MR due to the contribution of Hall conductance.

The corresponding MC under a perpendicular magnetic field can be analyzed with the simplified Hikami–Larkin–Nagaoka (HLN) equation [46],

$$\Delta\sigma_{xx}(B_\perp) \simeq -\alpha\frac{e^2}{2\pi^2\hbar}\left[\psi\left(\frac{1}{2}+\frac{\hbar}{4el_\phi^2 B_\perp}\right)-\ln\left(\frac{\hbar}{4el_\phi^2 B_\perp}\right)\right], \tag{1}$$

where $\Delta\sigma_{xx}(B) = \sigma_{xx}(B) - \sigma_{xx}(0)$. Here, $\psi(x)$ is the digamma function and α is a prefactor that is determined by the number of independent coherent channels. A single surface channel gives $\alpha = 0.5$, while two independent surface channels give $\alpha = 0.5 + 0.5 = 1.0$ Thus, given the value of α,

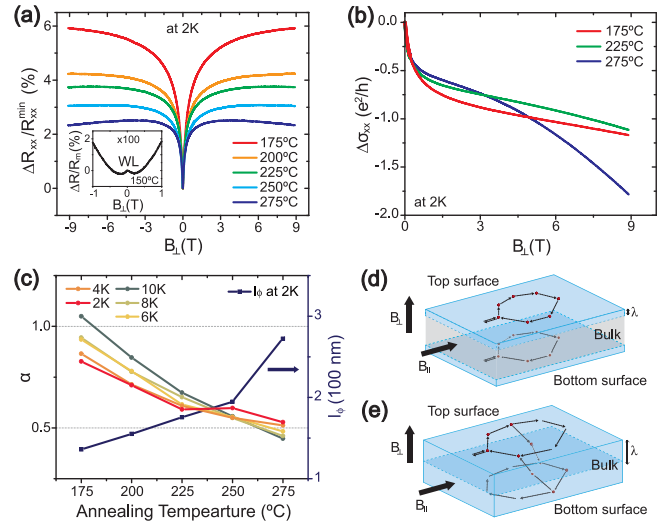

FIG. 3. WAL effect on the Bi_2Se_3 thin films under a magnetic field. (a) Magnetoresistance measurements under a perpendicular magnetic field for different annealing temperatures. The inset shows the WL effect for a film annealed at 150 °C. (b) The corresponding MC for different annealing temperatures. (c) Fitted results obtained with the HLN equation. The number of coherent channels is reduced as the annealing temperature is increased. Schematics outlining how TSS penetration and possible closed carrier trajectories can induce a WAL effect for (d) insulating and (e) doped TI films. Perpendicular and parallel magnetic fields pierce the regions penetrated by the TSSs and break the coherence.

we can identify whether a TI film has a single coupled channel owing to the inter-surface coupling, or two decoupled channels without intersurface coupling [14,16]. In the case where the two channels are partially coupled, the value of α is between 0.5 and 1.0. These changes in α due to indirect coupling are clearly distinguished from the situation where direct coupling is present for film thicknesses below 6 QL. The direct coupling creates a hybridization gap at the Dirac point, which produces a shift of π Berry phase and weakens the WAL effect, resulting in α decreasing to approximately zero [13]. Figure 3(c) shows the fitted results determined in accordance with the HLN equation. The fitting range of the magnetic field is chosen as [−0.2 T, 0.2 T], in which the magnetic length $l_B = \sqrt{\hbar/eB}$ is much longer than the mean free path, such that the HLN equation is considered to be valid [22,47]. The dependence of the fitting range is shown in Fig. S6. in the Supplemental Material [30]. From the fitted results, we find that α decreases as the annealing temperature is increased, which implies that the intersurface coupling is enhanced. Furthermore, the change of α from ∼1.0 to ∼0.5 indicates that two coherent channels exhibiting the WAL effect are reduced to a single coherent channel. Therefore, we can regard the disordered film as comprising two decoupled surface channels, while the ordered film has a single coupled surface channel, as commonly exhibited in doped TI thin films. Furthermore, α increases as the measurement temperature increases from 2 to 10 K for partially coupled films annealed below 250 °C. In particular, the temperature dependence of α reverses after the surface channels are fully coupled, as shown in Fig. 3(c). This temperature dependent

reversal is consistent with previously reported work [21] and will be discussed in the following.

However, it is important to note that when the Fermi energy is larger than the bulk band gap, the bulk states can also contribute to the WAL effect owing to strong spin-orbit coupling effects in TI materials [16]. In the case where the Fermi level is located near the conduction band edge, spin-momentum locking is reduced and the π Berry phase accumulated from the rotation of the spin along a closed path disappears. As a result, the bulk states thus exhibit a WL effect. In general, the WL effect of bulk states is not observed owing to strong surface–bulk coupling and the long phase coherence length of the TSSs [45]. Thus, a possible scenario to explain the increase in the prefactor α for the disordered film is that it is caused by contribution from the bulk states. To properly identify the origin of the WAL effect, we performed MC measurements on 100-QL-thick Bi_2Se_3 films annealed at different temperatures (see Fig. S8 and Table S1 in the Supplemental Material [30]). These films were sufficiently thick to decouple the top and bottom TSSs. If the bulk states contribute to the WAL effect, the resulting value of α would be $\sim$1.5 because of the existence of three coherent channels [24]. However, the value of α obtained from the HLN equation is approximately 1.0 for the 100-QL-thick Bi_2Se_3 film irrespective of the annealing temperature, which indicates that the larger value of α for the disordered film is due to the crossover between coupled surface channels and decoupled surface channels, and not due to a contribution from the bulk states.

We also observe that the phase coherence lengths for all 20-QL-thick films obtained in the 2–10 K temperature range are notably larger than the film thickness. Therefore, the Bi_2Se_3 thin films can be treated as 2D systems with regard to the quantum interference effect [45,48]. Theoretically, the temperature dependence of the coherence length in 2D systems exhibits a power law dependence, $l_\phi \sim T^{-0.5}$, which corresponds to the Nyquist 2D EEI decoherence mechanism [34,49], while the temperature dependence of the coherence length in 3D systems is $l_\phi \sim T^{-0.75}$. The fitted temperature dependence results, which are in the range, $l_\phi \sim T^{-0.47\sim-0.52}$, are consistent with a 2D system (see Fig. S5 in the Supplemental Material [30]).

C. WAL due to penetration of TSSs

Figures 3(d) and 3(e) describe how the penetration of TSSs and possible closed carrier trajectories with surface–bulk and inter-surface scatterings can determine the induction of WAL effect for insulating and doped TI films, respectively. The insulating TI film exhibits short TSS penetration due to weak surface–bulk coupling [16,19], which leads to coherent TSS carriers only residing near the surface region. Thus, closed loops in the top and bottom surfaces contribute independently to the WAL effect. However, the doped TI film exhibits strong surface–bulk coupling resulting in greater TSS penetration. If the penetration depth (λ) is sufficiently large, the TSS carriers can tunnel to the opposite surface without decoherence. This is the case of a coupled surface transport channel. We note that the WAL cusp owing to decoherence under a perpendicular magnetic field is only sensitive to the parallel motion of carriers, although the carriers can also undergo a perpendicular motion that induces intersurface coupling. Therefore, analysis

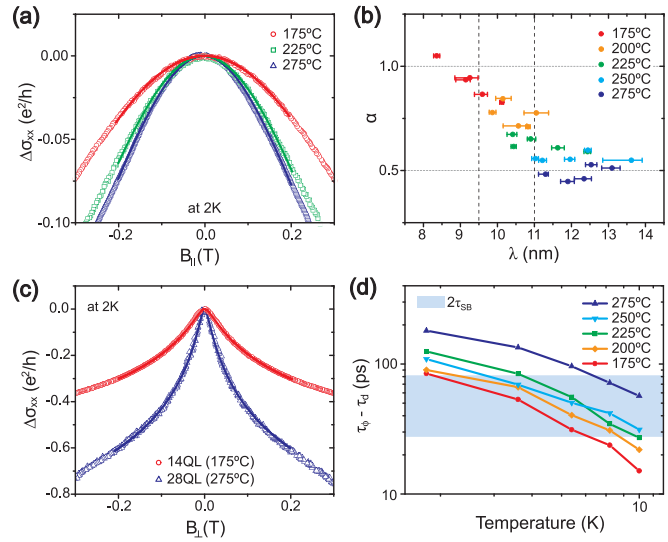

FIG. 4. (a) Magnified MC image showing the effects of WAL on Bi_2Se_3 thin films under a parallel magnetic field. (b) Fitted results obtained using Eq. (2). The WAL effect under a parallel field arises from the penetration of TSSs into the bulk states. The prefactor α is plotted as a function of the penetration depth, λ. (c) MC of the 14-QL-thick film annealed at 175 °C and 28-QL-thick film annealed at 275 °C which are slightly thinner and thicker than 2λ, respectively. (d) Estimation of the surface–bulk scattering time. Inter-surface coupling can occur when $(\tau_\phi - \tau_d) > 2\tau_{SB}$. Since the Fermi levels of our films are far from the conduction band edge, the difference in the surface–bulk scattering time does not depend significantly on the disorder.

of the WAL effect under a perpendicular magnetic field is not enough to provide a full understanding of the inter-surface coupling. With this in mind, we performed measurements of the MC under parallel magnetic fields and studied the observed WAL cusp, as shown in Fig. 4(a). The current was applied parallel to the magnetic field, with the result that the current direction does not affect the MC under parallel magnetic fields (see Fig. S7 in the Supplemental Material [30]).

In particular, the bulk states, TSSs on the side walls, and the penetration of the top and bottom TSSs into the bulk can be considered as possible causes of the WAL cusp under parallel magnetic fields [24,47]. The absence of a WAL effect arising from the bulk states can be verified from MC measurements for 100-QL-thick Bi_2Se_3 films under a perpendicular magnetic field. When a parallel magnetic field is applied, it pierces the side walls of the film and breaks the coherence of the TSSs along the side walls. However, when the phase coherence length is larger than the perimeter of film so that the coherence trajectories are long enough to wrap more than once around the film, the WAL effect arising from side wall TSSs is noticeable. But since this effect does not arise for TI films where the size of the film is larger than the coherence length [47], we can regard WAL effects arising from side wall TSSs in our films to be marginal. By the same principle, a parallel magnetic field pierces the region penetrated by the top and bottom TSSs and breaks their coherence, as shown in Fig. 3(e). Since the Fermi levels of our films are far from the conduction band edge (see Fig. S3 in the Supplemental Material [30]), the TSSs and bulk states are strongly coupled, which implies that the

TSSs penetrate deeply into the bulk states and the films exhibit a strong WAL cusp. Therefore, the change in conductivity of our films under a parallel magnetic field is comparable to that under a perpendicular field (see Fig. S7 in the Supplemental Material [30]). These results are thus clearly distinguished from those reported for insulating TI films where the change in conductivity under parallel fields is negligible [23,50].

The MC of the TI films under parallel magnetic fields was analyzed with the following equation by Tkachov and Hankiewicz [19], which is a modified form of the Altshuler and Aronov (AA) equation [51],

$$\Delta\sigma_{xx}(B_{\parallel}) \simeq -\alpha\frac{e^2}{2\pi^2\hbar}\ln\left[1+2\left(\frac{e\lambda l_{\phi,\perp}}{\hbar}\right)^2\cdot B_{\parallel}^2\right]. \quad (2)$$

Here, $l_{\phi,\perp} \approx l_{\phi}/\sqrt{3}$ is the coherence length in the perpendicular direction and can be estimated by fitted results with Eq. (1). After fitting the MC shown in Fig. 4(a) with Eq. (2), we can plot the prefactor α as a function of the penetration depth, as shown in Fig. 4(b). We find that the more ordered film has a longer penetration depth, and α increases from 0.5 to 1.0 as the penetration depth is decreased when $\lambda \leqslant 11$ nm, while α remains at 0.5 when $\lambda > 11$ nm. In other words, the coupled surface channel begins to decouple at $\lambda \approx 11$ nm, and becomes fully decoupled at $\lambda \approx 9$ nm. Ideally, one expects that the surface channels are decoupled when $2\lambda < d$, where d is thickness of the film [24], while the channels are coupled when $2\lambda > d$. Thus, the critical penetration depth, i.e., the crossover point between coupled and decoupled surface channels, is expected to be approximately 9.5 nm for a 20-QL-thick TI film. We note that our fitted result of 11 nm is slightly different to this ideal value because the estimated ratio of the coherence lengths in the perpendicular and parallel directions, obtained using previously reported results [41], is not a precise value. As we mentioned in our analysis of the Raman spectra, the crystallinity difference in direction was not the same for all TI films, which introduced some error in calculating the penetration depth. Nevertheless, the estimated results shown in Fig. 4(b) are sufficient to demonstrate the relation between the inter-surface coupling and the penetration depth. In addition, to clarify the relation between the penetration depth and the thickness of the film we performed MC measurements for 14- and 28-QL-thick films that were slightly thinner and thicker than 2λ, respectively. Figure 4(c) shows the MC of the 14-QL-thick film annealed at 175 °C and the 28-QL-thick film annealed at 275 °C. The α values are ~0.5 for 14 QL and ~1.0 for 28 QL, which indicates that a thickness of 2λ can be considered a suitable criterion for inter-surface coupling. The data and fitted results are presented in Fig. S9 and Table S2 in the Supplemental Material [30].

We can also estimate the intersurface coupling condition by comparing the phase coherence time (τ_{ϕ}) and intersurface tunneling time (τ_t), as in Fig. 4(e). Electrons can tunnel to the opposite TSS without dephasing provided that $\tau_{\phi} > \tau_t$, which leads to the coupling of the two surface channels [16,22,23]. The intersurface tunneling time is given by $\tau_t = 2\tau_{SB} + \tau_d$, where τ_{SB} is the surface–bulk scattering time, $\tau_d = d^2/D_{\perp}$ is the diffusion time across the film thickness, and $D_{\perp}$ is the diffusion constant in the perpendicular direction. The surface–bulk scattering time depends on the difference in momentum between electrons in the surface and bulk bands and is related to the shape of band structure and the position of the Fermi level [21]. Since the Fermi levels of our films are far from the conduction band edge, we can assume that the surface–bulk scattering time does not depend significantly on the amount of disorder present in the film [17]. However, the phase coherence time does depend significantly on the extent of disorder [22]. Therefore, by modulating the disorder, the intersurface coupling condition can be broken if we choose a suitable film thickness. We note that this crossover from coupled to decoupled surface channels is not observed for the 14- and 28-QL-thick films (see Fig. S9 and Table S2 in the Supplemental Material [30]). Furthermore, both the surface–bulk scattering time and the phase coherence time decrease with increasing temperature, however, since the scattering time varies more slowly, the decoupling process can be enhanced for partially decoupled TI films ($\alpha > 0.5$).

IV. CONCLUSIONS

We have shown that it is possible to induce decoupled surface channels in doped TI films through the modulation of disorder. The extent of disorder can be controlled successfully by suitable adjustment of the annealing temperature, as evidenced by our structural analyses. The crucial role of disorder in the decoupling process is its reduction of the phase coherence time. In more disordered films, the TSS carriers rapidly lose their quantum phase and coherence while tunneling to the opposite TSS, which leads to a shorter penetration of the TSS into the bulk states. We experimentally verified this mechanism in this report by studying the transport properties of doped TI films under both a perpendicular magnetic field and a parallel magnetic field, which were essential to thoroughly understand the intersurface coupling. In general, most studies regarding the role of disorder have been focused on its influence on the surface–bulk scattering [16,17,42,52], but our results indicate that the role of disorder must be considered as a source of decoherence. Many research groups are trying to utilize TI films in spintronic and quantum computation applications due to novel properties of TSSs. However, since disorder can critically affect the spin transport and dynamic properties of such devices, intensive research is required to understand the role of disorder and establish control of the intersurface coupling for the effective use of TI-based quantum devices, as well as for our understanding of transport mechanisms in TI films.

ACKNOWLEDGMENTS

This work was supported by the National Research Foundation of Korea (NRF) grant funded by the Korea government (MSIP) (Grant No. 2018R1A2A1A05023214) and by Samsung Research Funding Center of Samsung Electronics under Project No. SRFC-MA1502-01 and by the Korea Research Institute of Standards and Science (KRISS) under the Metrology Research Center project. The authors would like to thank Hee-Suk Chung at the Korea Basic Science Institute for technical assistance with STEM and Byeong-Gyu Park at the Pohang Accelerator Laboratory for technical assistance with ARPES.

[1] M. Z. Hasan and C. L. Kane, Rev. Mod. Phys. **82**, 3045 (2010).

[2] Y. Ando and I. R. Papers, J. Phys. Soc. Jpn. **82**, 102001 (2013).

[3] P. Roushan, J. Seo, C. V. Parker, Y. S. Hor, D. Hsieh, D. Qian, A. Richardella, M. Z. Hasan, R. J. Cava, and A. Yazdani, Nature **460**, 1106 (2009).

[4] D. Pesin and A. H. MacDonald, Nat. Mater. **11**, 409 (2012).

[5] A. R. Mellnik, J. S. Lee, A. Richardella, J. L. Grab, P. J. Mintun, M. H. Fischer, A. Vaezi, A. Manchon, E. A. Kim, N. Samarth, and D. C. Ralph, Nature **511**, 449 (2014).

[6] C. H. Li, O. M. J. van 't Erve, J. T. Robinson, Y. Liu, L. Li, and B. T. Jonker, Nat. Nanotechnol. **9**, 218 (2014).

[7] J. E. Moore, Nature **464**, 194 (2010).

[8] D. O. Scanlon, P. D. C. King, R. P. Singh, A. De La Torre, S. M. Walker, G. Balakrishnan, F. Baumberger, and C. R. A. Catlow, Adv. Mater. **24**, 2154 (2012).

[9] C.-X. Liu, H. J. Zhang, B. Yan, X.-L. Qi, T. Frauenheim, X. Dai, Z. Fang, and S.-C. Zhang, Phys. Rev. B **81**, 041307(R) (2010).

[10] H.-Z. Lu, W.-Y. Shan, W. Yao, Q. Niu, and S.-Q. Shen, Phys. Rev. B **81**, 115407 (2010).

[11] Y. Zhang, K. He, C.-Z. Chang, C.-L. Song, L.-L. Wang, X. Chen, J.-F. Jia, Z. Fang, X. Dai, W.-Y. Shan, S.-Q. Shen, Q. Niu, X.-L. Qi, S.-C. Zhang, X.-C. Ma, and Q.-K. Xue, Nat. Phys. **6**, 712 (2010).

[12] M. Neupane, A. Richardella, J. Sánchez-Barriga, S. Xu, N. Alidoust, I. Belopolski, C. Liu, G. Bian, D. Zhang, D. Marchenko, A. Varykhalov, O. Rader, M. Leandersson, T. Balasubramanian, T.-R. Chang, H.-T. Jeng, S. Basak, H. Lin, A. Bansil, N. Samarth, and M. Z. Hasan, Nat. Commun. **5**, 3841 (2014).

[13] A. A. Taskin, S. Sasaki, K. Segawa, and Y. Ando, Phys. Rev. Lett. **109**, 066803 (2012).

[14] M. Brahlek, N. Koirala, M. Salehi, N. Bansal, and S. Oh, Phys. Rev. Lett. **113**, 026801 (2014).

[15] H.-Z. Lu and S.-Q. Shen, Proc. SPIE **9167**, 91672E (2014).

[16] I. Garate and L. Glazman, Phys. Rev. B **86**, 035422 (2012).

[17] K. Saha and I. Garate, Phys. Rev. B **90**, 245418 (2014).

[18] W. Zhang, R. Yu, H.-J. Zhang, X. Dai, and Z. Fang, New J. Phys. **12**, 065013 (2010).

[19] G. Tkachov and E. M. Hankiewicz, Phys. Rev. B **84**, 035444 (2011).

[20] J. Chen, H. J. Qin, F. Yang, J. Liu, T. Guan, F. M. Qu, G. H. Zhang, J. R. Shi, X. C. Xie, C. L. Yang, K. H. Wu, Y. Q. Li, and L. Lu, Phys. Rev. Lett. **105**, 176602 (2010).

[21] H. Steinberg, J.-B. Laloë, V. Fatemi, J. S. Moodera, and P. Jarillo-Herrero, Phys. Rev. B **84**, 233101 (2011).

[22] D. Kim, P. Syers, N. P. Butch, J. Paglione, and M. S. Fuhrer, Nat. Commun. **4**, 2040 (2013).

[23] Z. Li, I. Garate, J. Pan, X. Wan, T. Chen, W. Ning, X. Zhang, F. Song, Y. Meng, X. Hong, X. Wang, L. Pi, X. Wang, B. Wang, S. Li, M. A. Reed, L. Glazman, and G. Wang, Phys. Rev. B **91**, 041401 (2015).

[24] A. Banerjee, O. Deb, K. Majhi, R. Ganesan, D. Sen, and P. S. A. Kumar, Nanoscale **9**, 6755 (2017).

[25] M. Brahlek, N. Koirala, M. Salehi, J. Moon, W. Zhang, H. Li, X. Zhou, M.-G. Han, L. Wu, T. Emge, H.-D. Lee, C. Xu, S. J. Rhee, T. Gustafsson, N. P. Armitage, Y. Zhu, D. S. Dessau, W. Wu, and S. Oh, Phys. Rev. B **94**, 165104 (2016).

[26] T.-H. Kim, K. Jeong, B. C. Park, H. Choi, S. H. Park, S. Jung, J. Park, K.-H. Jeong, J. W. Kim, J. H. Kim, and M.-H. Cho, Nanoscale **8**, 741 (2016).

[27] D. Kong, J. J. Cha, K. Lai, H. Peng, J. G. Analytis, S. Meister, Y. Chen, H.-J. Zhang, I. R. Fisher, Z.-X. Shen, and Y. Cui, ACS Nano **5**, 4698 (2011).

[28] M. Salehi, M. Brahlek, N. Koirala, J. Moon, L. Wu, N. P. Armitage, and S. Oh, APL Mater. **3**, 091101 (2015).

[29] J. Chen, X. Y. He, K. H. Wu, Z. Q. Ji, L. Lu, J. R. Shi, J. H. Smet, and Y. Q. Li, Phys. Rev. B **83**, 241304 (2011).

[30] See Supplemental Material at http://link.aps.org/supplemental/10.1103/PhysRevB.98.045411 for details of structural and electrical analysis.

[31] E. Schierle, Antiferromagnetism in thin films studied by resonant magnetic soft x-ray scattering, Ph.D. thesis, Freien Universität Berlin, 2006.

[32] L. He, F. Xiu, X. Yu, M. Teague, W. Jiang, Y. Fan, X. Kou, M. Lang, Y. Wang, G. Huang, N.-C. Yeh, and K. L. Wang, Nano Lett. **12**, 1486 (2012).

[33] Y. Zhao, H. Liu, X. Guo, Y. Jiang, Y. Sun, H. Wang, Y. Wang, H.-D. Li, M.-H. Xie, X.-C. Xie, and J. Wang, Nano Lett. **14**, 5244 (2014).

[34] B. L. Altshuler, A. G. Aronov, and D. E. Khmelnitsky, J. Phys. C **15**, 7367 (1982).

[35] D. S. Golubev, A. D. Zaikin, and G. Schön, J. Low Temp. Phys. **126**, 1355 (2001).

[36] J. G. Analytis, J.-H. Chu, Y. Chen, F. Corredor, R. D. McDonald, Z. X. Shen, and I. R. Fisher, Phys. Rev. B **81**, 205407 (2010).

[37] L. Veyrat, F. Iacovella, J. Dufouleur, C. Nowka, H. Funke, M. Yang, W. Escoffier, M. Goiran, B. Eichler, O. G. Schmidt, B. Büchner, S. Hampel, and R. Giraud, Nano Lett. **15**, 7503 (2015).

[38] Y. S. Kim, M. Brahlek, N. Bansal, E. Edrey, G. A. Kapilevich, K. Iida, M. Tanimura, Y. Horibe, S.-W. Cheong, and S. Oh, Phys. Rev. B **84**, 073109 (2011).

[39] M. Brahlek, N. Koirala, N. Bansal, and S. Oh, Solid State Commun. **215–216**, 54 (2015).

[40] J. Liao, Y. Ou, X. Feng, S. Yang, C. Lin, W. Yang, K. Wu, K. He, X. Ma, Q.-K. Xue, and Y. Li, Phys. Rev. Lett. **114**, 216601 (2015).

[41] M. Stordeur, K. K. Ketavonc, A. Priemuth, H. Sobotta, and V. Riede, Phys. Stat. Sol. **169**, 505 (1992).

[42] C. J. Lin, X. Y. He, J. Liao, X. X. Wang, V. Sacksteder IV, W. M. Yang, T. Guan, Q. M. Zhang, L. Gu, G. Y. Zhang, C. G. Zeng, X. Dai, K. H. Wu, and Y. Q. Li, Phys. Rev. B **88**, 041307(R) (2013).

[43] G. Bergmann, Phys. Rep. **107**, 1 (1984).

[44] D. Culcer, Physica E **44**, 860 (2012).

[45] J. H. Bardarson and J. E. Moore, Rep. Prog. Phys. **76**, 056501 (2013).

[46] S. Hikami, A. I. Larkin, and Y. Nagaoka, Prog. Theor. Phys. **63**, 707 (1980).

[47] V. E. Sacksteder, K. B. Arnardottir, S. Kettemann, and I. A. Shelykh, Phys. Rev. B **90**, 235148 (2014).

[48] C. W. J. Beenakker and H. van Houten, Quantum transport in semiconductor nanostructures, in *Solid State Physics*, Vol. 44 (Academic, New York, 1991), pp. 1–228.

[49] R. Dey, T. Pramanik, A. Roy, A. Rai, S. Guchhait, S. Sonde, H. C. P. Movva, L. Colombo, L. F. Register, and S. K. Banerjee, Appl. Phys. Lett. **104**, 223111 (2014).

[50] J. Lee, J. Park, J.-H. Lee, J. S. Kim, and H.-J. Lee, Phys. Rev. B **86**, 245321 (2012).

[51] B. L. Al'tshuler and A. G. Aronov, Pis'ma Zh. Eksp. Teor. Fiz. **33**, 515 (1981) [JETP Lett. **33**, 499 (1981)].

[52] D. L. Bergman and G. Refael, Phys. Rev. B **82**, 195417 (2010).